POLITECNICO DI TORINO
Repository ISTITUZIONALE

Investigating the relationship between geometry and hemodynamics in an experimentally derived murine coronary computational model

Original
Investigating the relationship between geometry and hemodynamics in an experimentally derived murine coronary computational model / Serafini, E., Martino, A., Sangiorgio, E., Bovetti, M., Corti, A., Fallon, B.C., Willson, R.C., Gallo, D., Chiastra, C., Li, X.C., Filgueira, C.S., Casarin, S.. - In: COMPUTERS IN BIOLOGY AND MEDICINE. - ISSN 0010-4825. - ELETTRONICO. - 187:(2025). [10.1016/j.compbiomed.2025.109793]

Availability:
This version is available at: 11583/2999350 since: 2025-04-18T12:37:45Z

Publisher:
Elsevier

Published
DOI:10.1016/j.compbiomed.2025.109793

Terms of use:

This article is made available under terms and conditions as specified in the corresponding bibliographic description in the repository

Publisher copyright

(Article begins on next page)

20 November 2026

Computers in Biology and Medicine 187 (2025) 109793



Contents lists available at ScienceDirect

Computers in Biology and Medicine

journal homepage: www.elsevier.com/locate/compbiomed



Investigating the relationship between geometry and hemodynamics in an experimentally derived murine coronary computational model

Elisa Serafini [a,b,1], Antonio Martino [c,d,1], Enrico Sangiorgio [a,e], Maddalena Bovetti [a,e], Anna Corti [f], Blake C. Fallon [c], Richard C. Willson [g], Diego Gallo [e], Claudio Chiastra [e], Xian C. Li [h,i], Carly S. Filgueira [c,j,k], Stefano Casarin [a,b,i,*]

[a] Center for Precision Surgery, Houston Methodist Research Institute, Houston, TX, 77030, USA
[b] LaSIE, UMR 7356, CNRS, La Rochelle Université, La Rochelle, 17000, France
[c] Department of Nanomedicine, Houston Methodist Research Institute, Houston, TX, 77030, USA
[d] Department of Material Science and Engineering, University of Houston, Houston, TX, 77204, USA
[e] Polito^{BIO}Med Lab, Department of Mechanical and Aerospace Engineering, Politecnico di Torino, Turin, 10129, Italy
[f] Department of Electronics, Information and Bioengineering, Polytechnic of Milan, Milan, 20133, Italy
[g] Department of Chemical and Biomolecular Engineering, University of Houston, Houston, TX, 77204, USA
[h] Immunobiology and Transplant Science Center, Houston Methodist Research Institute, Houston, TX, 77030, USA
[i] Department of Surgery, Houston Methodist Hospital, Houston, TX, 77030, USA
[j] Department of Cardiovascular Surgery, Houston Methodist Research Institute, Houston, TX, 77030, USA
[k] Department of Nanomedicine in Cardiothoracic Surgery, Weill Cornell Medicine, New York, NY, 10021, USA

ARTICLE INFO

Keywords:
Coronary artery disease
Murine models
X-ray microtomography
Microfil coronary perfusion
In silico modeling
Morphometric analysis
Hemodynamics

ABSTRACT

Despite the critical role of coronary morphology and hemodynamics in the development of coronary artery disease (CAD), comprehensive analyses of these factors in murine models are limited. Our study integrates *in vivo* approaches with computational methods to yield a complete set of precise and reliable morphologic and hemodynamic measurements and to investigate their interrelationship in the left coronary artery of healthy C57BL/6 mice. The work utilizes advanced micro-computed tomography imaging, enhanced with Microfil® coronary perfusion, complemented by morphometric analysis and computational fluid dynamic simulation. Our results in murine coronary arteries show: i) bifurcations are the most geometrically complex regions, susceptible to disturbed hemodynamics and, consequently, endothelial dysfunction; ii) vascular endothelial cells experience wall shear stress (WSS) an order of magnitude greater than in humans, primarily due to their smaller size, although minimal WSS multi-directionality is noted in both species; iii) intravascular flow exhibits reduced helical patterns compared to human coronaries, indicating a need for further investigation into their potential protective role against disease onset; and iv) strong correlations between geometric and hemodynamic indices highlight the need to integrate these factors for a comprehensive understanding of CAD initiation and progression in preclinical models. Thus, to optimize research based on murine models, it is essential not only to move beyond idealized geometries, but also to avoid uncritically relying on hemodynamic measurements from different species. This study grounds future development of mouse-specific predictive models of CAD, a critical step toward advancing translational research to understand and prevent CAD in humans.

1. Introduction

Coronary artery disease (CAD) is a major cause of mortality and morbidity [1]. While the early and acute stages of CAD can be managed with conservative therapies such as lifestyle changes and medications to delay disease progression, these approaches often prove ineffective in severe cases (i.e., when multiple coronaries are narrowed by $\geq$ 50 %). Procedures, such as percutaneous coronary intervention (PCI) or coronary artery bypass grafting (CABG), are then necessary to restore normal blood flow [2,3]. However, long-term outcomes of PCI and CABG

* Corresponding author. Center for Precision Surgery, Houston Methodist Research Institute, Houston, TX, 77030, USA.
E-mail address: SCasarin@houstonmethodist.org (S. Casarin).
[1] These authors contributed equally to the work.

https://doi.org/10.1016/j.compbiomed.2025.109793
Received 9 October 2024; Received in revised form 29 January 2025; Accepted 31 January 2025
0010-4825/Published by Elsevier Ltd. This is an open access article under the CC BY-NC license (http://creativecommons.org/licenses/by-nc/4.0/).

remain suboptimal; patients frequently progress to end-stage heart failure and require heart transplantation [2]. Post-transplant, patients face challenges including the risk of rejection, with mortality rates at 1, 5, and 10 years reported as 5.2 %, 15.9 %, and 27.7 %, respectively [4]. A leading cause of rejection is cardiac allograft vasculopathy (CAV), a condition characterized by graft coronary artery lumen narrowing due to intimal hyperplasia. CAV significantly contributes to chronic rejection, affecting approximately 25 % of post-transplant patients at 5 years and 50 % at 10 years [5]. Effective treatments for CAV are limited and diagnosis generally occurs only at advanced stages when symptoms become apparent, often too late for successful therapeutic intervention [6].

Given the broad spectrum of CADs and their significant impacts on patient well-being, there is an urgent need to optimize current therapies. *In vivo* pre-clinical studies are extensively used in this area as they can recapitulate physical and biological complexity and provide standardized, reproducible, experimental conditions for investigating pathophysiological mechanisms, testing therapies, and supporting translational research overall [7]. In particular, rodents are widely used in cardiovascular research [7] due to their ability to replicate diverse conditions and disorders such as models of heart failure after induced myocardial infarction [8–11], ischemic cardiomyopathy via diet-induction [12], and transplant tolerance and rejection [12,13]. Mice are preferred due to our ability to manipulate their genomes [14], test the relationships between specific genetic or protein markers and mechanisms of disease and repair (e.g., gene expression databases), and perform a wide variety of behavioral and histological assessments [15]. Moreover, *in vivo* experiments provide data that can be harnessed for further development of *in silico* models, which offer valuable platforms to optimize and complement traditional *in vivo* cardiovascular research [16]. With the rise of physics-based simulations and machine learning models [17], using *in silico* models to predict the effects of physiological factors on hemodynamics will likely transform the field of CAD pharmacotherapy.

Making comprehensive morphometric and hemodynamic measurements in the coronary arteries of mouse models is essential for CAD translational research. Specifically, investigating the features of the left coronary artery (LCA) is crucial, since it supplies blood and nutrients to the largest and most critical portion of the heart (i.e., the left ventricle), and it is the most prone to develop vascular abnormalities that lead to myocardial dysfunction [18,19]. The interplay between vessel geometry and hemodynamic indices provides key insights into the complex mechanisms of CAD initiation and progression, thus advancing our understanding of the pathophysiology and aiding in the development of more effective therapies [20]. The literature provides extensive documentation regarding coronary vessel measurements from arteries to capillaries in large animal models such as pigs, highlighting the role of geometry in controlling blood flow patterns [21–24]. The hemodynamics of mouse aortas have been successfully characterized, due to the relative ease of measurements at this location [25–28]. However, a comprehensive set of both anatomical measurements (e.g., vessel diameter and bifurcation angle) and hemodynamic indices (e.g., wall shear stress and intravascular flow metrics) from murine coronary arteries is lacking, mainly due to their small vessel size, which requires high resolution imaging, and to the dataset variability, which makes it challenging to standardize data and draw direct comparisons.

Recent advancements in computed tomography (CT) techniques, along with improved acquisition protocols and reconstruction algorithms, have greatly advanced anatomical evaluation and longitudinal monitoring in diverse preclinical applications [29–32]. In particular, micro-computed tomography (micro-CT) enables the visualization of fine anatomical structures [33], especially when combined with radiopaque agents that enhance contrast and resolution [34]. This combination, followed by cutting-edge computational reconstruction techniques, allows for non-destructive, high-precision imaging and accurate identification and measurement of anatomical structures such as coronary arteries in small animals such as mice [35–38]. These techniques utilize computational algorithms to distinguish between different tissue densities, identify anatomical landmarks, and enhance spatial resolution, such that detailed three-dimensional (3D) reconstructions can be generated. These reconstructions allow visualization of vascular architecture and accurate quantification of morphometric parameters, including vessel diameter, length, cross-sectional area, and bifurcation angles. Simultaneously, computational fluid dynamics (CFD) simulations have improved the study of hemodynamics by providing detailed analyses of blood flow patterns within different regions of the vascular system [39], including coronary arteries [40–42]. Several metrics can be extracted to quantify hemodynamics, such as wall shear stress (WSS), i.e., the frictional force exerted by the blood flow on the vessel endothelium, or helicity, i.e., the degree of coherence among the vortex lines in the blood flow. Both indicators have widely recognized roles in vascular pathophysiology [43,44].

In this work, we integrate advanced experimental and computational techniques to provide a unique and complete quantitative characterization of murine coronary geometry and hemodynamics. Accordingly, we developed an integrated protocol for micro-CT acquisition combined with computational methods, including image segmentation, morphometric analysis, and CFD simulation to establish and disseminate an extensive set of morphometric and hemodynamic measurements and their mutual relationship in a murine LCA model, addressing a critical gap in the literature.

Our ultimate objective is to strengthen the foundation for preclinical studies on CAD by further elucidating the complex relationship between coronary anatomy and pathology. Additionally, this research provides crucial data to integrate and validate predictive *in silico* models, advance alternative computational approaches in CAD research, and enhance our understanding of how coronary morphology and hemodynamics may be used to better predict CAD initiation and progression.

2. Materials and methods

The project workflow consisted of five phases: i) micro-CT imaging of murine heart samples after *ex vivo* 3D casting, ii) 3D reconstruction of the coronary vessels using segmentation techniques and subsequent LCA geometry optimization, iii) morphometric analysis of the extracted LCA structure, iv) CFD simulation within the LCA structure, and v) bivariate correlation analysis between geometrical measurements and hemodynamic descriptors.

2.1. Sample preparation and micro-CT imaging

An initial cohort of mice (C57BL/6 female mice, 5–8 weeks, ~16.5 g, n = 40, purchased from Taconic Biosciences [Rensselaer, NY, USA]) was sacrificed and the thoracic cavities exposed. A slit was made in the right atrium to allow for blood drainage, and a 23G x 75 inch BD Vacutainer® Safety-Lok™ Blood Collection Set (Becton, Dickenson and Company, Franklin Lakes, NJ, USA) was inserted apically along the coronal plane of the left ventricle. The hearts were first perfused with 15 mL of heparinized-saline solution (2000 units per 1 L) using a syringe pump at a rate of 0.75–1 mL/min to flush the entire circulatory system of blood, preventing clot formation and vessel rupture. To enhance the resolution of subsequent micro-CT imaging, we then perfused the hearts with Microfil® solution, a radiopaque polymer compound (MV-122 Yellow, Flow-Tek Inc., Cockeysville, MD, USA), which augments contrast in the mouse heart. For proper volume mixing and activation, the Microfil compound was combined with the manufacturer-supplied diluent in a 4:5 mL ratio, and a 5 % MV Curing Agent was incorporated to generate a 20–30 cP viscosity solution, which has a 20-min working time. The perfusion rate of the heparinized saline/Microfil solutions was carefully optimized to balance two critical factors: it needed to be slow enough to avoid disrupting or damaging the vessels while fast enough to prevent clotting (with the heparinized saline) and ensure complete perfusion

before the Microfil solution began to transition to an elastomeric gel. Once perfused, the samples were stored overnight at 4 °C to ensure complete curing of the Microfil, preserve organ viability with minimal cold injury, and maintain a consistent experimental timeline. This approach also prevented tissue degradation or necrosis by allowing for timely micro-CT imaging the following day. Hearts were extracted and fixed in 10 % formalin. For imaging, organs were transferred to 15 ml Falcon tubes (Fisher Scientific, Waltham, MA, USA) and suspended in 10 % formalin. Micro-CT imaging was performed using a SkyScan1276 (Bruker, Billerica, MA, USA) at 55 kV and 200 μA with 10 μm resolution, enabling acquisition of the entire myocardial vasculature system. CTVox software (Bruker, Kontich, Belgium) was used to visualize the acquired micro-CT DICOM-format images for preliminary examination to ensure adequate imaging settings and sample loading. From the initial cohort of 40 animals, 6 specimens were selected for further investigation based on successful perfusion and continuity of the vascular system. During the perfusion, we assessed for evidence of Microfil exiting the carotid artery (which was cut to allow blood drainage and depressurization) and for visible filling of the coronary arteries, including the main branches, as proof of complete vascular perfusion. Specimen selection was also made following visual inspection of the explanted hearts, micro-CT imaging, and 3D volume rendering of the vascular tree. Specimens lacking contrast or showing incomplete or discontinuous perfusion in the LCA were excluded. This research protocol was granted Institutional Animal Care and Use Committee (IACUC) approval (protocol #IS00005178, approved 6 May 2019) at the Houston Methodist Research Institute.

2.2. Segmentation, 3D vessel geometry reconstruction, and optimization

A dual-step segmentation approach was developed (Fig. 1) to reconstruct the 3D geometry of the coronary tree starting from acquired micro-CT DICOM images (Fig. 1A). This approach consists of two steps: i) the segmentation of the heart chambers performed using ITK-SNAP open access software (Insight Toolkit, Philadelphia, PA, USA; Fig. 1B) [45], facilitating ii) segmentation of the coronary tree using CT-Analyzer (CTAn) software (Bruker, Kontich, Belgium, provided by the micro-CT facility; Fig. 1C). Each program had limitations in directly segmenting the coronary tree (e.g., ITK-SNAP faced problems isolating coronary arteries, while CTAn faced challenges in removing the heart chambers). However, their combined use in a unified pipeline effectively addressed the issues, not only mitigating the shortcomings of each software alone, but also establishes a standardized, cost-effective, and time-efficient protocol for segmentation of murine coronary tree, avoiding the need for expensive commercially available software. From the coronary tree segmentation, the LCA was extracted (Fig. 1D) and optimized (Fig. 1E) through a routine to reduce the surface roughness. The LCA was prioritized for the study due to its significance in CAD research as a site of early vasculopathy manifestations [18,19].

Segmentation of the heart chambers involves two main phases: the pre-segmentation step and the 3D active contour initialization and evolution. During the pre-segmentation phase, the heart chambers are distinguished from the background using a thresholding function designed to capture regions with roughly uniform intensity. Further details of this process are provided in Supplementary Material S1.1. The 3D active contour phase begins by initializing 3D contours within the heart chambers. This process involves manual contour placement by the user and is crucial for ensuring adequate segmentation accuracy. Once positioned, the contours evolve actively through a combination of external regional competition forces and internal smoothing forces, acting perpendicular to the contour. Evolution is allowed to continue until the entire area of the heart chamber is identified. To prevent the contours from expanding into the coronary tree region, the operator stops the process based on visual observation.

Segmentation of the coronary tree involves two sequential steps. The first focuses on processing the raw micro-CT data, incorporating thresholding, bitwise operations, and despeckle functions. A high-pass thresholding function with a cut-off intensity I_t is defined to identify the heart chambers and coronary vessels, thereby producing a binary image. To isolate the coronary vessel tree, a Boolean-based subtraction operation is implemented between the binary segmentation stack obtained from the ITK-SNAP software and the binary images from the CTAn analyses. The obtained 3D coronary tree mask undergoes further despeckle routine analyses to remove minor impurities. Segmentation returns a set of disconnected volumes, the largest of which corresponds to the main artery of the coronary vessel tree, while smaller volumes represent terminal fragments of small arteries. To refine the segmentation, a second task list is applied to retain only the first k set (i.e., the largest segmented volumes). The parameters I_t and k were set with a dedicated rationale provided in Supplementary Material S1.2.

The LCA geometries extracted from the reconstructed coronary trees next underwent a series of preparatory steps for subsequent morphometric analysis and CFD simulation. The initial steps, including LCA extraction and local smoothing, were carried out using SpaceClaim software (2023R2, ANSYS Inc., Canonsburg, PA, USA). Subsequent processing, including global smoothing and opening of inlet/outlet sections, were performed using the Vascular Modeling Toolkit (VMTK) software (Orobix Srl, Bergamo, Italy) [46]. To extract the LCA, vessels unconnected to the LCA were removed while those attached were separated at the LCA junction. The extracted LCA geometry, which initially had rough surfaces due to segmentation, were manually processed with a smoothing tool to normalize the superficial geometry. Local operations were repeatedly applied to smooth the vessel surface,

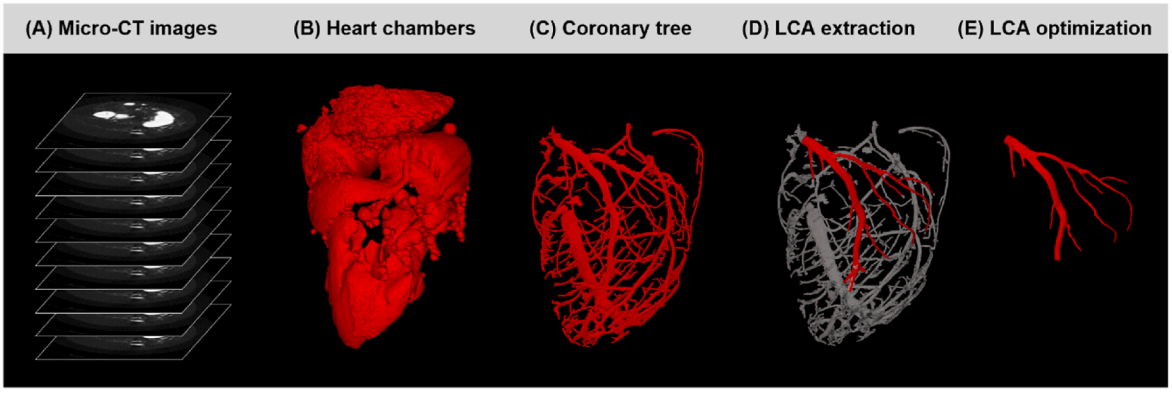


Fig. 1. Micro-CT image segmentation and 3D vessel geometry reconstruction. (A) Micro-CT images of C57BL/6 mouse hearts (image pixel size 10 μm). 3D reconstructions of (B) heart chamber volume and (C) coronary tree, obtained through a two steps segmentation approach. Left Coronary Artery (LCA) (D) extraction and (E) optimization based on a smoothing routine to facilitate morphometric analyses and computational fluid dynamics simulations.

ensuring that the displacement of surface points remained within a maximum of 2.5 % relative to the original geometry. Subsequently, a global spatial Taubin filter [47] was applied to further reduce and increase the uniformity of the surface roughness of the vessels. This involves adjusting two main parameters: the low-pass filter cut-off frequency f_l and the number of smoothing iterations n_s, as detailed in Supplementary Material S1.3. Once the combination of local and global smoothing steps was completed, the inlet and outlet sections of the LCA were opened by clipping and removing the endcaps. Details on the computational times of 3D reconstruction operations, including segmentation and geometry optimization, are given in Supplementary Material S1.4.

2.3. Morphometric analysis

A centerline-based morphometric analysis [48] was conducted on the LCA geometries (n = 6) retrieved by the methods of Section 2.2 to extract the following geometric parameters: curvature (κ), torsion (τ), tortuosity (T), in-plane bifurcation angle between Left Anterior Descending (LAD) and Left Circumflex (LCx) coronary arteries ($\gamma_{LAD-LCx}$), mean diameter ($\overline{D}$), and cross-sectional area (CSA). The latter are summarized in Table 1. The discrete centerline was automatically computed in VMTK as the geometrical locus of the centers of the maximal inscribed spheres in the vascular geometry by initially placing its source point at the inlet section followed by target points at the outlet sections for the entire coronary tree, including its individual branches.

The calculations of κ, τ, and T, were affected by intrinsic noise in the 3D centerline discrete estimation. To address this, we employed an analytical formulation in MATLAB software (R2023b, MathWorks, Natick, MA, USA) of the centerline implementing the 3D free-knots regression spline technique that reduces the oscillation between data points by interpolation [49]. The number and position of knots were optimized to minimize error, ensuring consistency between the discrete and analytical formulations [50] before computing κ, τ, and T (Table 1). Further details on the centerline optimization process can be found in Supplementary Material S2.1. κ, τ and T were used to statistically analyze the correlation between geometric features and hemodynamic indexes, presented in Section 2.5.

The calculation of the bifurcation angle $\gamma_{LAD-LCx}$ was conducted to characterize the LAD-LCx bifurcation among the datasets. We considered each bifurcation to be composed of three elements: the mother vessel (Left Main Coronary Artery, LMCA), upstream of the centerline separation, and two downstream daughter vessels (LAD and LCx). Using VMTK, we identified the bifurcation plane (i.e., the location whereby the daughter vessels depart from the mother vessel) and established a bifurcation reference system, comprised of the normal vector of the bifurcation plane, the mother-daughter vector, and their cross product. The in-plane projection angles (α and β) of both the mother and daughter vessels were utilized to compute $\gamma_{LAD-LCx}$ (Table 1). Each bifurcation was further characterized by additional geometric measurements such as $\overline{D}$ (the average of the minimum and maximum diameters of the vessel's section) and CSA (area of the considered section) of mother and daughter vessels. We employed VMTK to extract the branch section at 2x the radius length distance from the bifurcation (equivalent to one inscribed sphere), calculate $\overline{D}$, and subsequently, determine CSA. This approach ensured standardized and comprehensive measurements across all bifurcations. $\overline{D}$ values were used to classify LCA segments according to the diameter-defined Strahler system [21] to run an intra- and inter-model analysis. Details about the Strahler system classification are provided in Supplementary Material S2.2. Briefly, each sample was divided into multiple segments, whereby each segment was assigned to an order number between 1 and 4 according to diameter range definitions where for O1: $\overline{D} < 0.091\ mm$; O2: $0.091\ mm < \overline{D} < 0.144\ mm$; O3: $0.144\ mm < \overline{D} < 0.218\ mm$; and O4: $0.218\ mm < \overline{D} < 0.267\ mm$.

By comparing the LCA reconstruction with the *ex vivo* heart images acquired with a stereo-dissecting microscope (Olympus SZX10, Evident Scientific, Inc., Waltham, MA, USA), we ensured the reliability and robustness of our morphometric analysis. Fig. 2 outlines the three main steps of the consistency check protocol, presented in detail for Sample 1 (S1). This protocol involves overlapping the two objects of interest (i.e., *in silico* and *ex vivo* models; Fig. 2A), and identifying the reference points (Fig. 2B, yellow squares) using CloudCompare software [52], to finally conduct the *ex vivo* diameter measurements in Fiji software [53] (Fig. 2C, red line). The diameter $\overline{D}$ extracted *in silico* using VMTK was compared with the *ex vivo* diameter measured at each couple of reference points, through root mean square error (RMSE) calculation. The use of reference points ensured that *ex vivo* measurement positions accurately corresponded with the *in silico* measurement positions along the vessels, thereby minimizing positional errors and allowing for a more accurate and meaningful RMSE comparison.

Table 1
Geometric parameters for morphometric analysis.

Geometric Parameters			
Name	**Formula**	**Unit**	**Description**
Curvature (κ)	$\kappa = \frac{\lvert C'(s) \times C''(s) \rvert}{\lvert C'(s) \rvert^3}$	mm^{-1}	κ describes the amount by which a curve deviates from being a straight line in a 2D plane [48]
Torsion (τ)	$\tau = \frac{[C'(s) \times C''(s)] \bullet C'''(s)}{\lvert C'(s) \times C''(s) \rvert^2}$	mm^{-1}	τ describes the amount by which a curve deviates from being a straight line in a 3D space [48]
Tortuosity (T)	$T = 1 - \frac{D}{L}$	unitless	T describes abnormal twists and turns of the curve [51]
In-Plane Bifurcation Angle ($\gamma_{LAD-LCx}$)	$angle_{LAD-LCx} = \alpha + \beta$	degree	Angle formed by two former angles at the level of a vessel bifurcation [51]
Mean Diameter ($\overline{D}$)	N/A	mm	D describes the average of the minimum and maximum dimensions of a vessel's section, assuming it is not perfectly circular
Cross-Sectional Area (CSA)	N/A	mm^2	CSA describes the area of a section obtained by slicing the vessel surface with a plane orthogonal to its centerline

C', C'', C''': curvilinear abscissa first, second, third derivative; D: diameter; L: length; α and β: in-plane projection angles; N/A: not applicable.

2.4. CFD simulations

The optimized LCA geometries (n = 6), with the addition of a five-radius length flow extension ($l_{FE} = 5 \bullet \bar{r}_{inlet}$) to the inlet [46], were discretized with tetrahedral volume elements and five prismatic boundary layers near the vessel wall to capture near-wall velocity gradients. The mesh (approx. element face area: 1.53E-11 m^2) was generated using Ansys Fluent (2023R2, ANSYS Inc., Canonsburg, PA, USA), applying a curvature-based refinement control, guided by parameters derived from mesh sensitivity analysis detailed in Supplementary Material S3.1.

Blood was modeled as a homogenous, incompressible fluid with a constant density (ρ) equal to 1060 kg/m^3 and a viscosity (μ) following non-Newtonian behavior as described by the Carreau model [54]. Coefficients of the Carreau power law were retrieved by error minimization between the Carreau curve and murine μ-shear rate ($\dot{\gamma}$) data available in the literature [55,56]. Further details and a complete list of coefficients are provided in Supplementary Material S3.2.

The following boundary conditions (BCs) were prescribed: i) a flat and transient velocity profile at the inlet, with a mean velocity (V_{mean}) waveform derived from mouse Doppler ultrasound images [57] and

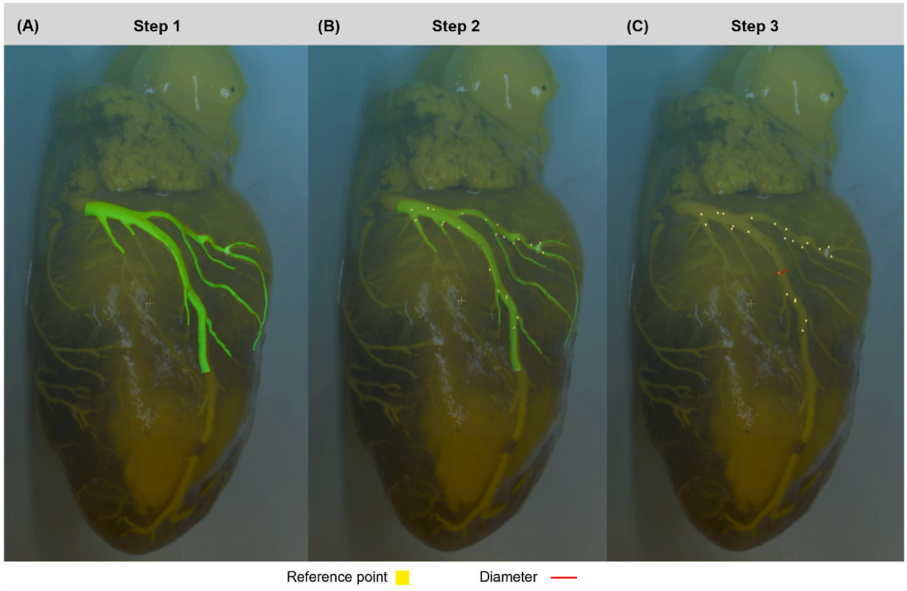


Fig. 2. Consistency check protocol presented on Sample 1 (S1). (A) Step 1 involves overlapping the *in silico* 2D view of Left Coronary Artery (LCA) (highlighted in yellow) with the *ex vivo* 2D microscope image (opaque). (B) Step 2 presents *in silico* reference points (yellow squares) along the LCA to accurately define the location for the diameter measurement. (C) Step 3 provides the localization of the reference points on the *ex vivo* microscope image to perform the diameter calculation (red segment). (For interpretation of the references to color in this figure legend, the reader is referred to the Web version of this article.)

scaled for each sample to ensure a fixed average blood flow rate (Q) of 0.30 ml/min [58,59] during a cardiac cycle; ii) a flow-split at the outlets, estimated by application of mass conservation equation and a flow-diameter scaling law based on the minimum energy hypothesis [60,61] and, iii) a no-slip condition applied to the wall, considered as a rigid structure. Further details about inlet and outlet BCs are provided in Supplementary Material S3.3. We conducted unsteady-state CFD simulations to replicate blood flow under laminar conditions over two cardiac cycles. Each cycle had a period T = 118 ms, corresponding to a high heart rate HR ≅ 508 beats/min [55,58,62]. These cycles were

Table 2
Hemodynamic descriptors for Computational Fluid Dynamic (CFD) simulations.

Hemodynamic Descriptors			
Name	**Formula**	**Unit**	**Description**
Time-Average Wall Shear Stress (TAWSS)	$TAWSS = \frac{1}{\mathrm{T}}\int_0^{\mathrm{T}} \left\lvert \overrightarrow{WSS} \right\rvert \bullet dt$	Pa	Averaged magnitude of the WSS vector over a cardiac cycle. Low WSS values promote inflammatory cell activation and subsequent endothelial dysfunctions, while extremely high values are associated with plaque vulnerability and rupture [43]
Oscillatory Shear Index (OSI)	$OSI = 0.5 \bullet \left[1 - \left(\frac{\left\lvert \int_0^{\mathrm{T}} \overrightarrow{WSS} \bullet dt \right\rvert}{\int_0^{\mathrm{T}} \left\lvert \overrightarrow{WSS} \right\rvert \bullet dt}\right)\right]$	unitless	A measure of the directional change of WSS vector during the cardiac cycle, accounting for the degree of flow reversal. OSI ranges from 0 (completely unidirectional WSS vector) to 0.5 (purely oscillatory WSS vector) [63]
Relative Residence Time (RRT)	$RRT = \frac{1}{TAWSS \bullet (1 - 2 \bullet OSI)}$	Pa^{-1}	Function of TAWSS and OSI. It identifies vessel wall regions simultaneously exposed to low and high oscillatory WSS (i.e., high atherogenic solutes residence time) [64]
Transverse Wall Shear Stress (transWSS)	$transWSS = \frac{1}{\mathrm{T}}\int_0^{T} \left\lvert \overrightarrow{WSS} \bullet \left(\vec{n} \times \frac{\int_0^{\mathrm{T}} \overrightarrow{WSS} \bullet dt}{\left\lvert \int_0^{\mathrm{T}} \overrightarrow{WSS} \bullet dt \right\rvert} \right) \right\rvert$	Pa	Average WSS vector component acting orthogonal to the cardiac-cycle-averaged WSS vector direction. High transWSS values are associated with maladaptive vessel remodeling [65]
Topological Shear Variation Index (TSVI)	$TSVI = \sqrt{\frac{1}{\mathrm{T}}\int_0^{\mathrm{T}} \left[DIV_{WSS_n} - \overline{DIV_{WSS_n}}\right]^2 dt}$	m^{-1}	The root mean square deviation of the divergence of the normalized WSS vector ($\mathrm{WSS_n}$). It quantifies the variability of WSS contraction/expansion action over a cardiac cycle. High TSVI values indicate regions susceptible to early pathological changes [66]
Local Normalized Helicity (LNH)	$LNH = \frac{\vec{v} \bullet \vec{\omega}}{\lvert\vec{v}\rvert \bullet \lvert\vec{\omega}\rvert} = \cos\varphi$	unitless	Measure of the alignment of local velocity and vorticity vectors. It ranges from −1 to +1, where values near ±1 correspond to strong helical flow and values close to 0 indicate weak helical flow. Positive/negative sign of LNH indicates right/left-handed helix rotation, respectively [43]
Average Helicity Intensity (h_2)	$h_2 = \frac{1}{\mathrm{T}}\frac{1}{V}\int_{\mathrm{T}}\int_V \lvert\vec{v} \bullet \vec{\omega}\rvert \, dV \, dt$	$\mathrm{m} \bullet \mathrm{s}^{-2}$	Measure of the cardiac-cycle-averaged helicity intensity in a reference volume. High h_2 values are potentially protective for atherosclerotic plaque buildup and low h_2 values are suggestive of endothelium regions experiencing proatherogenic WSS [67]

T: cardiac cycle time within the temporal variable t spans; $\overrightarrow{WSS}$: wall shear stress vector; WSS_n: normalized WSS (i.e., WSS vector divided by its magnitude); DIV_{WSS_n}: divergence of normalized WSS; $\vec{v}$: velocity vector; $\vec{\omega}$: vorticity vector; φ: $\vec{v}$ - $\vec{\omega}$ formed angle.

discretized into 100 time steps, resulting in a time step size of 1.18 ms and an overall simulation time of 236 ms. The governing equations for fluid motion were solved numerically using the finite volume-based software Ansys Fluent (2023R2, ANSYS Inc., Canonsburg, PA, USA). Solution methods and controls, along with the solution convergence conditions, are detailed in Supplementary Material S3.4.

To analyze near-wall and intravascular hemodynamics, we focused on the WSS distribution and velocity field results from the second simulated cardiac cycle. WSS-based hemodynamic descriptors were extracted to characterize the stress state imposed on the mouse LCA endothelium by the flowing blood. Specifically, Time-Averaged Wall Shear Stress (TAWSS), Oscillatory Shear Index (OSI), Relative Residence Time (RRT), transverse WSS (transWSS), and Topological Shear Variation Index (TSVI) were calculated. Additionally, helicity-based hemodynamic descriptors were extracted to characterize the intravascular features in terms of helical flow in the mouse LCA. Specifically, Local Normalized Helicity (LNH) and intensity of helical flow h_2 were computed. Both classes of these descriptors are summarized in Table 2.

2.5. Bivariate correlation analysis

For geometric-hemodynamic correlation, each vessel tree was split into segments excluding the bifurcation regions. For each LCA segment, the most meaningful geometric and hemodynamic descriptors, presented in Tables 1 and 2 respectively, were retrieved. In detail, mean curvature ($\bar{\kappa}$), mean torsion ($\bar{\tau}$), and tortuosity (T) were extracted as geometric features. No specific assumptions were made during the calculation of the geometric descriptors. These metrics were computed as described in Section 2.3, with each LCA segment analyzed individually along its centerline. The mean values of curvature ($\bar{\kappa}$) and torsion ($\bar{\tau}$) were calculated along the length of the centerline. LCA segments shorter than the 0.5 mm cut-off threshold were excluded from the analysis due to insufficient length for reliable geometric measurements. Further details regarding the choice of the 0.5 mm threshold are provided in Supplementary Material S4.1. The exclusion criteria reduced the dataset from 108 to 52 segments. However, only 30 % of the original superficial points (1,583,899 points vs. 1,109,746 points) were excluded. While the exclusion of shorter segments may introduce some bias, we focused on retaining a high proportion of superficial points for our analysis. Hemodynamic features were retrieved, i.e., median TAWSS, OSI, RRT, transWSS, and TSVI (medTAWSS, medOSI, medRRT, medtransWSS, medTSVI) and percentage of luminal area exposed to critical values, namely lower than the 33rd percentile for TAWSS (TAWSS33%) and higher than the 66th percentile for all other near-wall descriptors (OSI66%, RRT66%, transWSS66%, TSVI66%) [68]. Due to diameter variability among LCA segments, specific sets of critical thresholds were extracted for each Strahler order by analyzing the distribution of WSS-based indices across the segments assigned to that order. The values of the critical thresholds are listed in Supplementary Material S4.2. Additionally, the h_2 index was included as a hemodynamic feature. Spearman rank-based bivariate correlations among geometric, WSS-based, and helicity-based parameters were then computed to describe their relationships using MATLAB software (R2023b, MathWorks, Natick, MA, USA). Spearman's correlation was selected for this analysis due to its robustness in handling non-linear, monotonic relationships and its insensitivity to outliers, making it particularly suitable for data which may not follow a normal distribution or exhibit linearity. False Discovery Rate (FDR) correction was used to adjust p-values and control the ratio of false discoveries across multiple comparisons. We chose FDR over more conservative approaches (e.g., the Bonferroni method) because it provides a better balance between detecting meaningful correlations and controlling false positives, without overly increasing the risk of missing true relationship. Significance was indicated as follows: $^{*}p \leq 0.05$, $^{\dagger}p \leq 0.01$, $^{\ddagger}p \leq 0.001$.

3. Results

3.1. Microfil perfusion and 3D vessel geometry visualization

Fig. 3 presents stereo microscope images of *ex vivo* Microfil-perfused hearts (Fig. 3A) with the corresponding reconstructed 3D geometry of the coronary tree (Fig. 3B) and optimized 3D model of the LCA, including its main branches, such as LAD and LCx (Fig. 3C). The use of a radiopaque casting solution markedly enhanced the visualization of the vasculature compared to the cardiac tissue, enabling precise computer-based reconstruction of the entire coronary tree, even preserving detailed features of individual branches, such as the LCA. Qualitatively, some variability was observed in the 3D reconstructions of the entire coronary tree and shapes of the LCA across samples S1 to S6.

3.2. Morphometric analysis results and consistency check

The values of κ, τ, and T were obtained for all centerline points across the LCA geometries (n = 6). The κ values ranged from 0 to 8 mm^{-1}, with values exceeding 5 mm^{-1} along pronounced curvilinear tracts, values between 1 and 5 mm^{-1} at bifurcations, and the rest of the points (greater than 65 %) exhibiting κ below 1 mm^{-1}, as shown in Fig. 4. The τ values were predominantly near 0 along the entire centerline, with only occasional (less than 1 %) positive and negative peaks, and abrupt changes in direction ($|\tau| > 20$ mm^{-1}) indicated as highlighted in Fig. 4. High values of κ and τ at or adjacent to bifurcations suggested that these regions exhibit the highest levels of geometrical complexity. T values were calculated for the main branches of the LCA structure, such as LAD (median: 0.142, Q1: 0.130, Q3: 0.148) and LCx (median: 0.185, Q1: 0.148, Q3: 0.217), excluding S4 and S5 due to their short length (below 0.5 mm). The higher T value of the LCx compared to the LAD underscored the more tortuous, diagonally oriented geometry of the LCx, in contrast to the simpler, vertically oriented geometry of the LAD.

The in-plane bifurcation angle $\gamma_{LAD-LCx}$, along with the angles α and β formed between the LMCA mother vessel and LAD/LCx daughter vessels, are reported in Fig. 5A. Angle values were presented for each sample as well as median and interquartile range (α: median 15.48°, Q1 8.08°, Q3: 22.38°; β: median 41.98°, Q1 35.16°, Q3 47.20°; $\gamma_{LAD-LCx}$: median 57.46°, Q1: 53.43°, Q3: 65.81°). Across the LCA geometries, the β angle generally exhibited higher values compared to α, indicating and confirming a more twisted geometry for LCx compared to LAD, particularly at the bifurcation level.

The evaluation of the bifurcations, using the diameter-defined Strahler system across all the LCA geometries (n = 6), revealed that the order increases from the outlets towards the inlet of the LCA structure (Fig. 5B). Moreover, the side branch segments at the outlet, assigned to the lowest orders (O1, O2), exhibited the smallest $\overline{D}$ and *CSA*, while LCA inlet and LAD segments, assigned to the highest order (O3, O4), had the largest $\overline{D}$ and *CSA*. This branching pattern was consistent across all samples except for S4, where segments classifiable as O1 were removed during the endcap clipping step of the LCA optimization routine. In addition, the intra- and inter-model analyses of $\overline{D}$, averaged over the cross-sections of the same Strahler order, confirmed that $\overline{D}$ increases with increasing Strahler order within each sample (Fig. 5C) and showed that the range of $\overline{D}$ for each specific order remains consistent across all LCA samples (Fig. 5D).

The $\overline{D}$ measurements were utilized for the consistency check of the 3D vessel reconstructions. The analysis revealed low RMSE across the LCA geometries (median: 0.007 mm, Q1: 0.006 mm, Q3: 0.009 mm), confirming that the reconstructed model accurately replicates the *ex vivo* samples.

3.3. CFD simulation results

Fig. 6 displays WSS-based (back and front view) and helicity-based

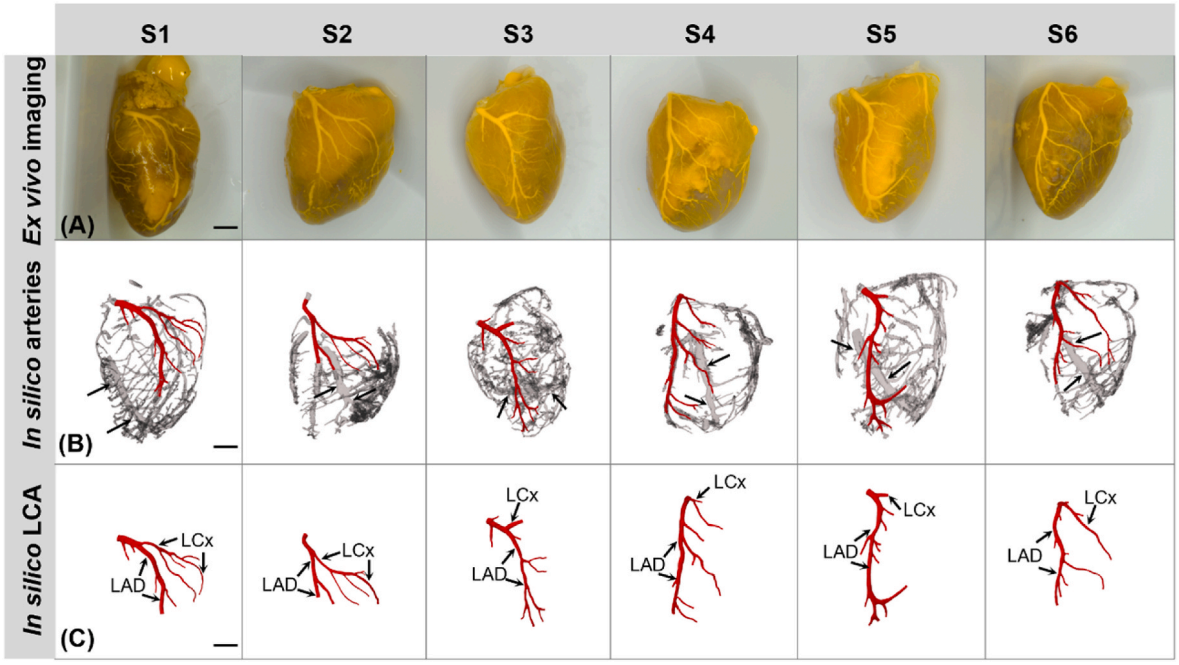


Fig. 3. Comparison between *ex vivo* and *in silico* geometry. (A) Mouse heart after perfusion of Microfil® visualized through *ex vivo* stereo microscopy imaging. (B) 3D *in silico* reconstruction of the mouse coronary tree with the Left Coronary Artery (LCA) highlighted in red and the Right Coronary Artery (RCA) indicated by black arrows. (C) 3D *in silico* optimized reconstruction of the mouse LCA with the left anterior descending (LAD) and the left circumflex (LCx) arteries indicated by black arrows. S1: sample 1; S2: sample 2; S3: sample 3; S4: sample 4; S5: sample 5; S6: sample 6. Scale bar: 1 mm. (For interpretation of the references to color in this figure legend, the reader is referred to the Web version of this article.)

(one view only) descriptors for a representative coronary tree sample, S1. Hemodynamic descriptors for all the other samples are provided in Supplementary Material S5. TAWSS values across the LCA geometries (median: 13.72 Pa, Q1: 9.38 Pa, Q3: 20.56 Pa) resulted in elevated hemodynamic stresses on mouse coronary endothelial cells. As expected, the highest WSS and TAWSS values were observed in the smallest branches of the LCA samples, where mean diameters are less than 80 μm (Fig. 6A). Moreover, analysis of TAWSS distribution, segregated by Strahler order, showed decreasing median values with increasing average diameter: 21.01 Pa (O1), 14.91 Pa (O2), 10.08 Pa (O3), and 7.08 Pa (O4).

OSI (median 2.02E-06, Q1: 0.40E-06, Q3: 7.84E-06) and transWSS (median: 0.03 Pa, Q1: 0.01 Pa, Q3: 0.07 Pa) values indicated limited multidirectional WSS in the mouse coronary arteries (Fig. 6B–D). Consequently, RRT (median 0.07 Pa^{-1}, Q1: 0.05 Pa^{-1}, Q3: 0.11 Pa^{-1}) essentially inversely mirrors TAWSS distribution and provides limited additional information into mouse coronary hemodynamics (Fig. 6C). TSVI values (median: 75.79 mm^{-1}, Q1: 34.61 mm^{-1}, Q3: 149.77 mm^{-1}) revealed greater variability in contraction and expansion actions exerted by WSS on endothelium in bifurcation regions compared to other lumen areas (Fig. 6E).

The LNH (±0.02) iso-surfaces revealed two discernible counter-rotating helical flow structures, with a well-defined symmetric arrangement along the main branch as well as smaller and less organized helical flow structures in the side branches (Fig. 6F). To quantitatively evaluate these intravascular flow patterns, the h_2 index was computed using the LCA segments as reference volumes to perform the correlation analysis (see Section 2.5), resulting in a median value of 7.72 ms^{-2} (Q1: 4.74 ms^{-2}, Q3: 18.07 ms^{-2}).

3.4. Bivariate correlation of geometry and hemodynamics

Spearman's rank correlation coefficients between each pair of geometric-geometric, geometric-hemodynamic, and hemodynamic-hemodynamic descriptors are summarized in Table 3, and the six most meaningful relationships are depicted in Fig. 7 using scatter plots. For the purpose of correlation analysis, we used mean values of the parameters (e.g., $\bar{\kappa}$, $\bar{\tau}$). However, when discussing the overall behavior or significance of these parameters, we referred to them using their general nomenclature (e.g., κ, τ). The statistical analysis revealed a strong, positive correlation between T and $\bar{\kappa}$ of the mouse LCA segments ($r = 0.80, p < 0.001$), indicating that κ is the primary factor contributing to the deviation of the segment centerline from a straight line (Fig. 7A). No other significant associations were found among the considered geometric parameters. Moreover, $\bar{\kappa}$ was the only geometric feature exhibiting a statistically significant correlation with hemodynamic metrics in the mouse LCA: $\bar{\kappa}$ was associated with OSI66% ($r = 0.37, p < 0.05$; Fig. 7B), TSVI66% ($r = 0.35, p < 0.05$; Fig. 7C), and medTSVI ($r = 0.49, p < 0.001$; Fig. 7D). Conversely, $\bar{\tau}$ and T showed no significant correlations with the percentages of segmented area exposed to disturbed flow patterns or to the median values of WSS-based quantities. Additionally, none of the geometric features extracted for each mouse LCA segment were found to be associated with the h_2 index. A total positive correlation was observed between TAWSS33% and RRT66% ($r = 1, p < 0.001$) as well as a total negative correlation between the median values of TAWSS and RRT ($r = -1, p < 0.001$). This evidence supported the hypothesis that RRT calculation is markedly biased by TAWSS value, with a negligible influence of OSI, in the mouse LCAs. The absence of statistically significant correlation between all the parameters associated with RRT and OSI (i.e., OSI66%, RRT66%, medOSI, medRRT) provided further confirmation. Interestingly, a strong positive correlation was observed for OSI66% with both transWSS66% ($r = 0.93, p < 0.001$) and TSVI66% ($r = 0.91, p < 0.001$) as well as for transWSS66% with TSVI66% ($r = 0.95, p < 0.001$). The evidence that these three WSS-based descriptors (i.e., OSI, transWSS, TSVI) are positively related was further corroborated by the correlation coefficient values between OSI66% and medtransWSS ($r = 0.92, p < 0.001$), OSI66% and medTSVI ($r = 0.84, p < 0.001$), and transWSS66% and medTSVI ($r = 0.86, p < 0.001$). Furthermore, the data indicates that larger surface areas exposed to low WSS corresponded to smaller surface

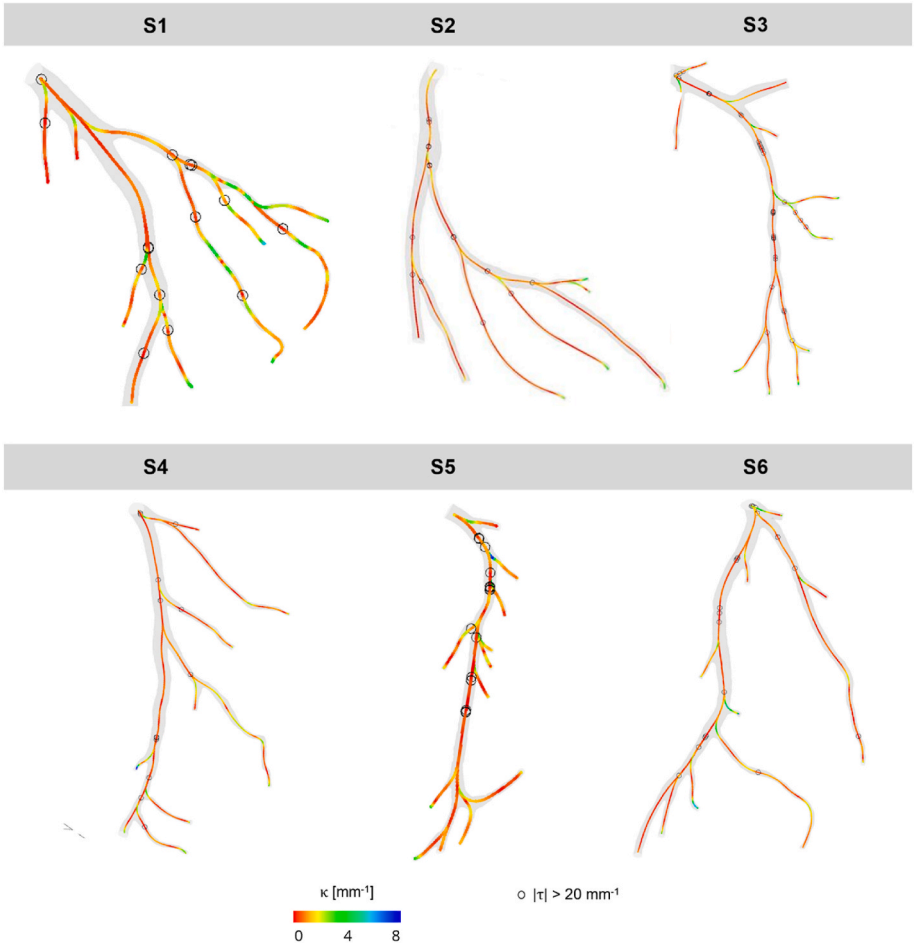


Fig. 4. Curvature (κ) and torsion (τ) calculation results. Colormaps show values of $\kappa \in [0–8]$ mm^{-1} and open black circles highlight values where $|\tau| > 20$ mm^{-1}, among the six Left Coronary Artery (LCA) samples. S1: sample 1; S2: sample 2; S3: sample 3; S4: sample 4; S5: sample 5; S6: sample 6.

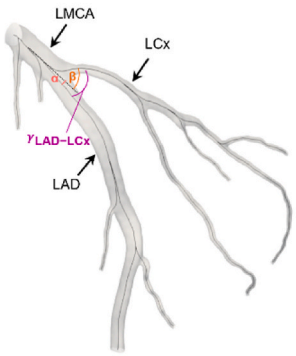
areas exposed to multidirectional WSS or high variability in the normalized WSS divergence, as evidenced by the moderate negative associations of TAWSS33% with transWSS66% ($r = -0.54, p < 0.001$) and TSVI66% ($r = -0.51, p < 0.001$), respectively. Finally, the correlation analysis also revealed significant associations between helicity-based and WSS-based descriptors. Specifically, h_2 showed the same negative correlations with both TAWSS33% (Fig. 7E) and RRT66% ($r = -0.69, p < 0.001$; Fig. 7G), indicating that the greater the cardiac-cycle-averaged helicity intensity within a LCA segment, the less luminal area is exposed to low WSS. In contrast, positive correlations were observed between h_2 and OSI66% ($r = 0.78, p < 0.001$; Fig. 7F), transWSS66% ($r = 0.90, p < 0.001$; Fig. 7H), and TSVI66% ($r = 0.87, p < 0.001$; Fig. 7I), suggesting that the higher the intensity of intravascular helical flow structures, the greater the LCA surface exposed to multidirectional WSS. To summarize the relationship between h_2 and WSS-based metrics: decreasing trends are appreciable between h_2 and both TAWSS33% and RRT66%, while increasing trends are found between h_2 and OSI66%, transWSS66%, and TSVI66%. However, in interpreting these results, it is important to note that in all LCA samples investigated, the multidirectional character of WSS is negligible and does not significantly impact local hemodynamics, as observed in Section 3.3.

4. Discussion

Murine models have significantly advanced our understanding of CADs [14]. However, a complete overview of the roles and relationships of geometry and hemodynamics remain elusive. In this study, we employed Microfil perfusion in conjunction with micro-CT imaging to create high-resolution 3D reconstructions of the murine coronary tree. This methodology builds upon previous approaches used for similar purposes, allowing for detailed visualization and analysis of coronary vasculature [58,69]. Our geometric reconstructions revealed differences in the vessel shapes and orientations across mice, aligning with previous studies and confirming the variability of mouse coronary geometries [70]. Although LAD and LCx were consistently identified across all six LCAs, we observed variations in their branching patterns and bifurcation angles. Individual anatomical variations among mice are expected, given the fractal nature of the coronary vasculature [71,72]. However, the observed geometrical variability may also be partially attributed to minor differences in the execution of the vasculature perfusion process, a concern that has also emerged in previous studies [35].

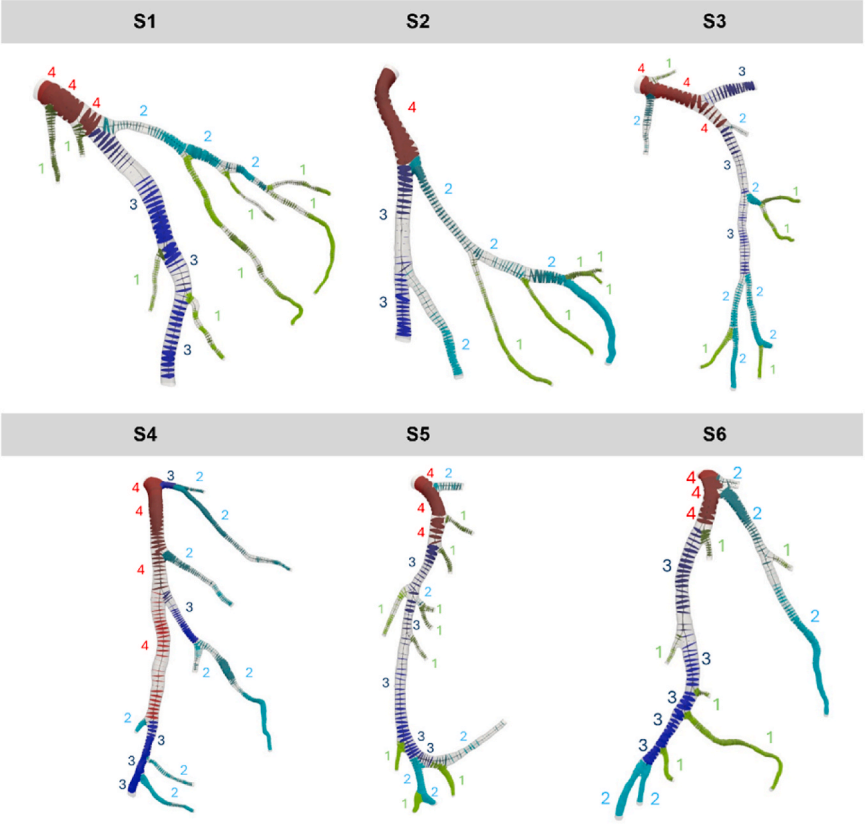
We supported these visual observations with a comprehensive morphometric analysis of the murine LCA. This analysis not only included vessel diameters and angles—which have been extensively studied in other animals, such as pigs [22], dogs [73], and rabbits [74]—but also highlighted critical geometrical features, such as curvature, torsion, and tortuosity, which have primarily been explored in pigs and humans [24]. Inter-species differences between mice and larger animals emerged in the geometrical assessments. Specifically, our results demonstrated that both the murine LAD and LCx arteries have a smaller caliber compared to their porcine counterparts. Murine LAD is characterized by a diameter range of 0.144–0.267 mm (considering O3 and O4 sections; Fig. 5B–D), whereas porcine LAD spans from 0.310 to 0.860 mm [22]. Similarly, murine LCx is defined within 0.091–0.144 mm (considering O1 and O2 sections; Fig. 5B–D), while the porcine LCx

(A)

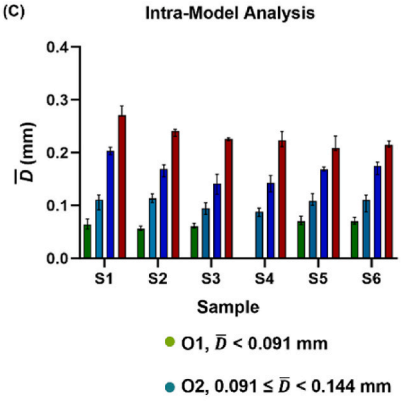


Sample	α	β	γLAD–LCx
S1	7.978°	33.32°	41.29°
S2	21.20°	32.19°	53.39°
S3	28.01°	40.69°	68.69°
S4	4.497°	52.67°	57.17°
S5	22.77°	47.88°	70.66°
S6	8.398°	45.14°	53.54°
Median	15.47°	41.98°	57.46°
Q1	8.08°	35.16°	53.43°
Q3	22.38°	47.20°	65.81°

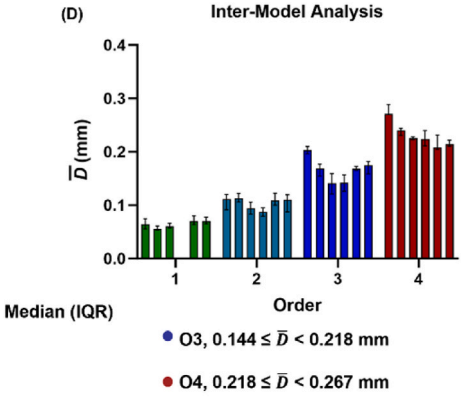
(B)



(C)



(D)



(caption on next page)

Fig. 5. In-plane bifurcation angle and diameter-defined Strahler system. (A) Sample S1 highlighting the in-plane bifurcation angle $\gamma_{LAD-LCx}$ between Left Anterior Descending (LAD) and Left Circumflex (LCx) arteries as well as the mother-daughter formed angles, α and β. Values for each sample, median and first-third quartile (Q1, Q3) for $\gamma_{LAD-LCx}$, α and β. (B) Diameter-defined Strahler system classification in four orders according to the mean diameter ($\overline{D}$) range definition for all samples. Mean and interquartile range (IQR) of $\overline{D}$ analyzed within each sample via intra-model analysis (C) and across all samples via inter-model analysis (D). Specific colors distinguish the Strahler orders (O1: green, O2: light blue, O3: blue, O4: red). O1: order 1, O2: order 2, O3: order 3, O4: order 4; S1 sample 1; S2: sample 2; S3: sample 3; S4: sample 4; S5: sample 5; S6: sample 6. (For interpretation of the references to color in this figure legend, the reader is referred to the Web version of this article.)

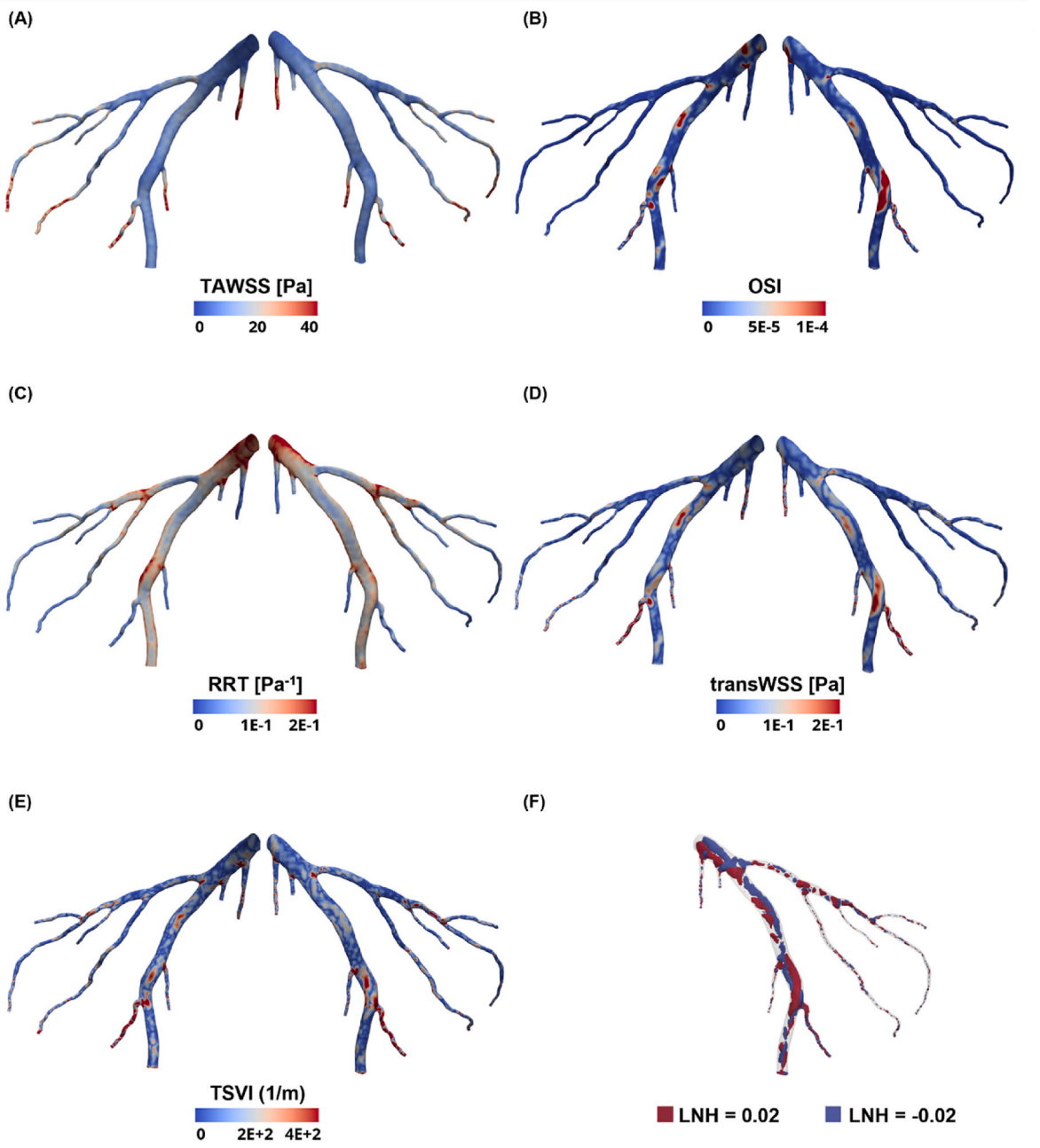


Fig. 6. Wall Shear Stress (WSS) and helicity-based hemodynamic descriptors for Sample 1 (S1). (A) Time Averaged Wall Shear Stress (TAWSS), (B) Oscillatory Shear Index (OSI), (C) Relative Residence Time (RRT), (D) Transverse Wall Shear Stress (transWSS), (E) Topological Shear variation Index (TSVI) with back (left) and front (right) views for superficial descriptors, and (F) Local Normalized Helicity (LNH) with only front view for the volumetric descriptor.

ranges from 0.590 to 1.300 mm [22]. Furthermore, comparing murine LAD/LCx curvature and torsion with those of pigs and humans revealed that these measurements are also higher in larger species. Specifically, murine curvature and torsion are on order of magnitude lower than pigs and humans, which share same orders of magnitude (curvature: 10^0 vs 10^1, torsion: 10^1 vs 10^2) [24]. Additionally, our analysis of the bifurcation angles between the LMCA and the LAD/LCx showed that the LCx consistently forms a larger angle with the LMCA. This can be attributed to the diagonal orientation of the LCx, in contrast to the vertical alignment of the LAD.

We complemented our geometric findings with a detailed hemodynamic analysis of the murine LCA, addressing a significant gap in the

Table 3
Spearman's rank correlation coefficients.

	$\bar{\kappa}$	$\bar{\tau}$	T	TAWSS33%	OSI66%	RRT66%	transWSS66%	TSVI66%	medTAWSS	medOSI	medRRT	medtransWSS	medTSVI	h_2
$\bar{\kappa}$	–	−0.13	**0.80**‡	0.16	0.37*	0.16	0.27	0.35*	0.30	0.01	−0.30	0.27	0.49‡	0.12
$\bar{\tau}$		–	−0.29	−0.06	−0.09	−0.05	−0.05	−0.09	0.07	−0.01	−0.07	−0.03	−0.06	0.02
T			–	0.15	0.23	0.15	0.15	0.21	0.23	−0.03	−0.23	0.14	0.30	0.03
TAWSS33%				–	−0.29	**1**†	−0.54‡	−0.51‡	−0.53‡	−0.18	0.53‡	−0.54‡	−0.48‡	**−0.69**‡
OSI66%					–	−0.29	**0.93**‡	**0.91**‡	0.24	**0.75**‡	−0.24	**0.92**‡	**0.84**‡	**0.78**‡
RRT66%						–	−0.54‡	−0.52‡	−0.53‡	−0.18	0.53‡	−0.55‡	−0.48‡	**−0.69**‡
transWSS66%							–	**0.95**‡	0.36*	**0.72**‡	−0.36*	**0.98**‡	**0.86**‡	**0.90**‡
TSVI66%								–	0.42†	**0.65**‡	−0.42†	0.95‡	**0.93**‡	**0.87**‡
medTAWSS									–	−0.28	**−1**‡	0.38*	**0.61**‡	0.58‡
medOSI										–	0.28	**0.71**†	0.43†	0.49†
medRRT											–	−0.38*	**−0.61**‡	−0.58‡
medtransWSS												–	**0.88**‡	**0.89**‡
medTSVI													–	**0.83**‡
h_2														–

* $p_{value} < 0.05$; † $p_{value} < 0.01$; ‡ $p_{value} < 0.001$. Spearman correlation coefficients with high absolute values ($|r| > 0.6$) are in bold.

literature, which has primarily focused on the hemodynamic investigation of larger mouse arteries, such as the aorta [24]. The small size of murine coronary arteries complicates their 3D reconstruction and the extrapolation of blood flow measurements, presenting challenges for investigating their hemodynamics though CFD simulations. We observed that WSS and TAWSS in mice ($10^{1;}$ Fig. 6A) are one order of magnitude higher than pigs and humans (10^{0}) [24]. This aligns with allometric scaling principles, which indicate an inverse relationship between body mass and WSS. Specifically, previous studies identified a scaling exponent of approximately −0.375 for the aortic arch (i.e., $WSS \propto M^{-0.375}$), resulting in a twenty-fold difference in WSS, when comparing typical body masses of 25 g for mice and 75 kg for humans [75]. Our findings suggested that murine coronary endothelial cells exhibit different WSS sensitivity compared to those in larger species, not only for the higher WSS exerted on them but also because they experience high temporal WSS gradients during the cardiac cycle, due to the elevated heart rate in mice [58]. Moreover, as previous research has shown for pigs and humans [24], limited WSS multi-directionality (expressed in terms of low OSI and transWSS; Fig. 6B–D) was present also in murine coronary arteries, confirming that these descriptors are not hallmark features of the coronary vasculature. Finally, an overall inter-species equivalence in the intravascular flow is evident, characterized by two distinguishable counter-rotating helical flow patterns present in mice, pigs, and humans [24]. However, the threshold values necessary for visualizing LNH iso-surfaces in mice (±0.02 in Fig. 6F) are one order of magnitude lower than those commonly employed in the coronary arteries of pigs and humans (±0.2) [68]. This suggests that the helical flow structures are weaker in mice compared to larger species. This reduced helical flow can be explained by the Dean number, which is directly proportional to the Reynolds number and vessel diameter, and inversely proportional to the vessel curvature radius [76]. In the case of murine coronary arteries, the low Reynolds numbers (i.e., $Re < 100$ at the LCA inlet), combined with small and twisted geometries, result in small Dean numbers. This indicates that viscous forces dominate over the inertial ones, leading to less pronounced secondary flow effects. Conversely, similarities in the average helicity intensity (h_2) values between mice, pigs, and humans suggest that this phenomenon must be further investigated. When computing h_2 in mouse LCA segments, the small integration volumes resulted in values of the same order of magnitude as those in larger species (range between 10^{0} and 10^{1}). Therefore, additional research is needed for understanding the eventual protective role of helical flow even in small-volume coronary arteries such as murine arteries, as has been already demonstrated in pigs and humans [68].

We performed a bivariate correlation analysis to further investigate the relationship between geometry and hemodynamics, which serves as the ultimate goal of our study. The correlation analysis revealed that the mean curvature is the geometric parameter with the greatest influence on murine hemodynamics, showing significant statistical correlations with LCA surface areas exposed to critical descriptor thresholds (i.e., OSI and TSVI; Table 3 and Fig. 7B and C). This finding demonstrates the existence of a relationship between in-plane vessel morphology, captured by the curvature and near-wall blood flow patterns. Additionally, none of the geometric features were found to be correlated with the h_2 index, in both mice (Table 3) and swine [68], suggesting that the role of geometry in influencing the intensity of the helical flow patterns may be masked by the complex geometric features of the coronary tree and the time-varying nature of the coronary hemodynamics. Finally, the correlations between the near-wall shear stress descriptors (i.e., TAWSS, OSI, RRT, transWSS, TSVI; Table 3) agreed with those previously reported for pig [68] and human [24] coronary hemodynamics. Furthermore, the high correlation coefficients between h_2 and WSS-based descriptors supported the hypothesis, already introduced for larger animals [68] and different vascular regions [67], that helical flow serves as surrogate marker of exposure to disturbed flow patterns also in the murine coronary artery.

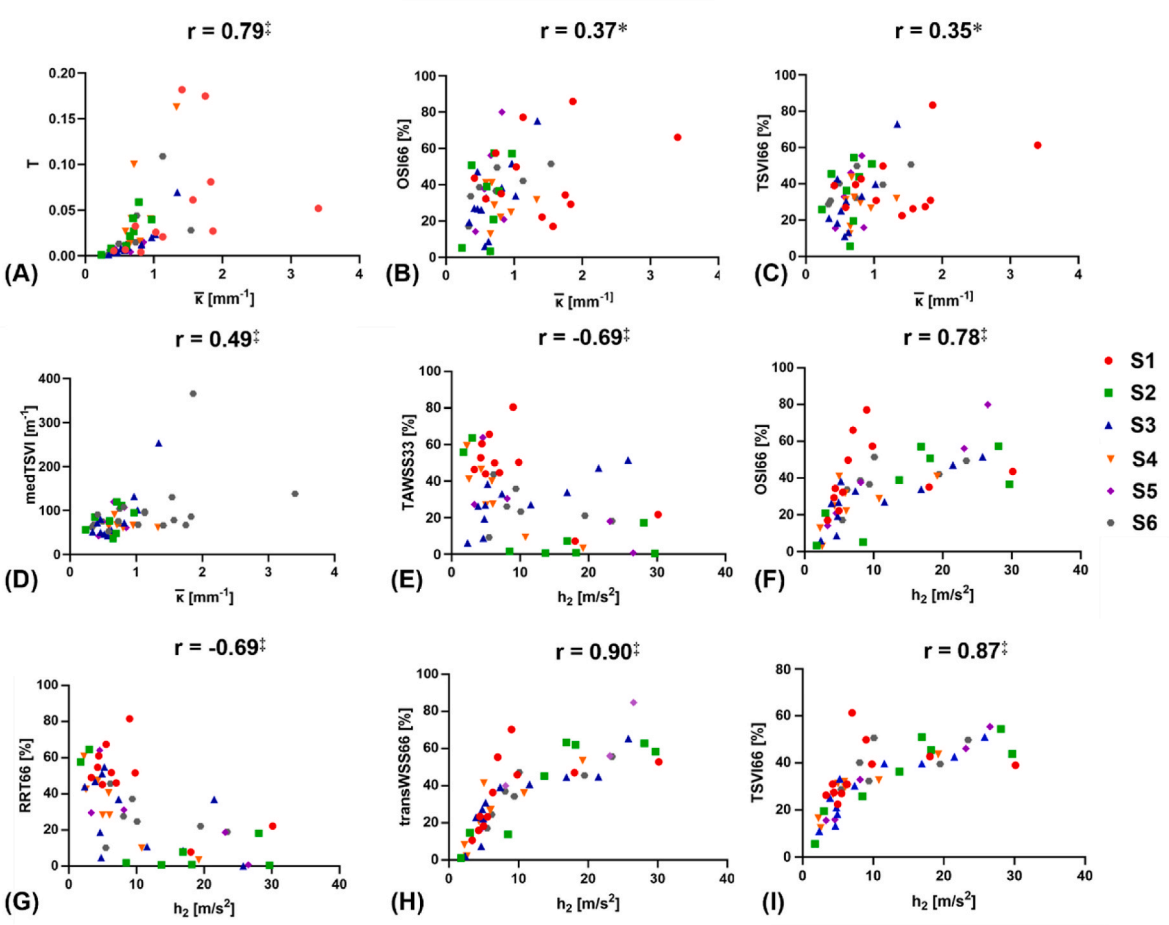


Fig. 7. Significant geometric-geometric, geometric-hemodynamic, and hemodynamic-hemodynamic correlations. Scatter plots of i) mean curvature ($\bar{\kappa}$) vs (A) tortuosity (T), (B) OSI66%, (C) TSVI66%, and (D) medTSVI, and of ii) helicity intensity (h_2) vs (E) TAWSS33%, (F) OSI66%, (G) RRT66%, (H) transWSS66%, and (I) TSVI66%. Different colors and symbols are used to differentiate data from distinct mouse left coronary artery (LCA) samples. S1: sample 1; S2: sample 2; S3: sample 3; S4: sample 4; S5: sample 5; S6: sample 6; * $p_{value} < 0.05$; † $p_{value} < 0.01$; ‡ $p_{value} < 0.001$. (For interpretation of the references to color in this figure legend, the reader is referred to the Web version of this article.)

In summary, the geometric and hemodynamic relationships observed in our analysis are consistent with findings from larger animal models, further supporting the validity of the metrics used to characterize the complexity of the coronary vasculature in murine models. To ensure the accuracy of these relationships, we conducted consistency checks on both morphometric and hemodynamic data. To guarantee the reliability of the geometry reconstruction and the related morphometric analysis, we compared the *in silico* LCA models with corresponding *ex vivo* images from the same subject. On the other hand, ensuring the reliability of CFD results would require verification, validation, and uncertainty quantifications. However, as geometry plays a pivotal role in shaping the flow, the main driver of reliable blood flow simulations is an accurate 3D reconstruction of the coronary artery lumen [77]. Another source of uncertainty arises from the boundary condition settings [78], which, due to the challenges in directly measuring flow rates in small animal models like mice, relied on commonly used methods in literature, allowing for comparison with other studies. Further robustness is provided by the agreement between our estimated WSS in LCA models and that predicted by the analytical formula for a rigid cylindrical tube under stationary laminal flow conditions. Moreover, the alignment with established allometric scaling laws provided confidence that our results accurately reflect the true physiological conditions and are not artifacts of the computational methods employed.

Some study limitations must be noted. First, the dataset size, which impacts the robustness of the statistical analysis, can be further expanded. Due to challenges with the Microfil perfusion and micro-CT acquisition, we successfully perfused and consequently acquired an entire, continuous vasculature for a small number of samples, ultimately selecting the final cohort for 3D geometry reconstruction (n = 6). Future efforts will focus on optimizing the vascular perfusion technique to improve overall outcomes, thus allowing analyses of a larger LCA dataset. Second, the segmentation and 3D vessel reconstruction phases involved time-consuming, manual, and operator-dependent functions, which are subject to human error, potentially altering vessel morphology. Future work will combine manual analysis with an adapted *in-house* deep learning neural networks-based architecture, which has been promising in automatic image segmentation to streamline and expedite the geometry reconstruction [79]. Third, the murine blood properties and the inlet BCs assigned to perform CFD simulations were derived from the literature, with the BCs specifically adapted to fit the geometry of each mouse. A future strategy will involve retrieving blood rheology and coronary flow measurements *in-house* prior to sacrifice, to increase consistency between reconstructed geometry, blood properties, and BCs for CFD simulation, thus adopting a mouse-specific approach.

5. Conclusion

This is the first study to provide a comprehensive set of morphological measurements, hemodynamic descriptors, and their interrelationships in a healthy, experimentally derived C57BL/6 mouse LCA model, addressing a notable gap in the cardiovascular pre-clinical research literature. Importantly, the work underscores how mouse

coronary blood properties and morphology, in terms of vessel shape and size, create a hemodynamic environment that, while sharing some similarities with larger animals and human coronary flow patterns (e.g., limited multidirectional WSS and the formation of two counter-rotating helical flow structures within the main branch), also show distinct differences, including higher WSS magnitude and lower helical flow strength. This work provides a solid foundation for further development of predictive mouse-specific models for CADs, serving as a physiological reference. Specifically, a key advancement will be integrating our previously published CAV agent-based model (ABM) [80] with the mouse-specific geometric features and CFD-derived hemodynamic input presented here. The ABM module will simulate cellular dynamics at the cellular level, while the CFD module will model the blood motion at the tissue level, revealing the complex interplay between different temporal and spatial scales that contribute to coronary disease manifestation.

CRediT authorship contribution statement

Elisa Serafini: Writing – review & editing, Writing – original draft, Visualization, Supervision, Methodology, Investigation, Formal analysis, Data curation, Conceptualization. **Antonio Martino:** Writing – review & editing, Writing – original draft, Visualization, Methodology, Investigation, Formal analysis, Data curation, Conceptualization. **Enrico Sangiorgio:** Writing – review & editing, Writing – original draft, Visualization, Software, Methodology, Investigation, Formal analysis, Data curation. **Maddalena Bovetti:** Visualization, Methodology, Formal analysis, Data curation, Conceptualization. **Anna Corti:** Writing – review & editing, Visualization, Data curation. **Blake C. Fallon:** Writing – review & editing, Visualization, Validation, Methodology, Investigation, Data curation. **Richard C. Willson:** Writing – review & editing, Supervision, Resources. **Diego Gallo:** Writing – review & editing, Validation, Supervision, Software, Methodology, Formal analysis. **Claudio Chiastra:** Writing – review & editing, Validation, Supervision, Software, Methodology, Formal analysis. **Xian C. Li:** Validation, Supervision, Resources. **Carly S. Filgueira:** Writing – review & editing, Visualization, Supervision, Resources, Methodology, Investigation, Funding acquisition, Formal analysis, Data curation, Conceptualization. **Stefano Casarin:** Writing – review & editing, Writing – original draft, Visualization, Validation, Supervision, Resources, Methodology, Investigation, Formal analysis, Data curation, Conceptualization.

Ethics statement

All procedures related to this research were performed in compliance with relevant laws and institutional guidelines and have been approved by the internal institutional committee. This research protocol was granted Institutional Animal Care and Use Committee (IACUC) approval (protocol #IS00005178, approved 6 May 2019) at the Houston Methodist Research Institute.

Declaration of generative AI and AI-assisted technologies in the writing process

During the preparation of this work the authors used DeepL Translate to proofread English. After using this tool/service, the authors reviewed and edited the content as needed and take full responsibility for the content of the publication.

Funding

ES and SC were supported by the John F. Jr. and Carolyn Bookout Presidential Distinguished Chair fund. CSF was supported by the George and Angelina Kostas Research Center for Cardiovascular Medicine and funded by Houston Methodist Research Institute. AC was funded by the National Plan for NRRP Complementary Investments (PNC, established with the decree-law 6 May 2021, n. 59, converted by law n. 101 of 2021) in the call for the funding of research initiatives for technologies and innovative trajectories in the health and care sectors (Directorial Decree n. 931 of 06-06-2022) - project n. PNC0000003 - AdvaNced Technologies for Human-centrEd Medicine (project acronym: ANTHEM). This work reflects only the authors' views and opinions; neither the Ministry for University and Research nor the European Commission can be considered responsible for them.

Declaration of competing interest

The authors declare no conflict of interest.

Acknowledgements

The authors thank Jacob M. Kolman, MA, ISMPP CMPP™, senior scientific writer (Houston Methodist Academic Institute) for linguistic review of the revised version of this manuscript.

Appendix A. Supplementary data

Supplementary data to this article can be found online at https://doi.org/10.1016/j.compbiomed.2025.109793.

References

[1] A. Kr Malakar, D. Choudhury, B. Halder, P. Paul, A. Uddin, S. Chakraborty, A review on coronary artery disease, its risk factors, and therapeutics, J. Cell. Physiol. 234 (10) (2019) 16812–16823, https://doi.org/10.1002/jcp.28350.
[2] T. Doenst, H. Thiele, J. Haasenritter, T. Wahlers, S. Massberg, A. Haverich, The treatment of coronary artery disease, Dtsch. Ärztebl. Int. 119 (42) (Oct. 2022) 716–723, https://doi.org/10.3238/arztebl.m2022.0277.
[3] C.S. Filgueira, et al., Technologies for intrapericardial delivery of therapeutics and cells, Adv. Drug Deliv. Rev. 151–152 (2019) 222–232, https://doi.org/10.1016/j.addr.2019.02.006.
[4] L.H. Lund, et al., The registry of the international society for heart and lung transplantation: thirty-fourth adult heart transplantation report-2017; focus theme: allograft ischemic time, J. Heart Lung Transplant. 36 (10) (Oct. 2017) 1037–1046, https://doi.org/10.1016/j.healun.2017.07.019.
[5] M. Perch, et al., The International Thoracic Organ Transplant Registry of the International Society for Heart and Lung Transplantation: thirty-ninth adult lung transplantation report-2022; focus on lung transplant recipients with chronic obstructive pulmonary disease, J. Heart Lung Transplant. 41 (10) (Oct. 2022) 1335–1347, https://doi.org/10.1016/j.healun.2022.08.007.
[6] B. Skorić, et al., Cardiac allograft vasculopathy: diagnosis, therapy, and prognosis, Croat. Med. J. 55 (6) (Dec. 2014) 562–576, https://doi.org/10.3325/cmj.2014.55.562.
[7] J. Liao, W. Huang, G. Liu, Animal models of coronary heart disease, J. Biomed. Res. 31 (1) (Jan. 2017) 3–10, https://doi.org/10.7555/JBR.30.20150051.
[8] R. Klocke, W. Tian, M.T. Kuhlmann, S. Nikol, Surgical animal models of heart failure related to coronary heart disease, Cardiovasc. Res. 74 (1) (Apr. 2007) 29–38, https://doi.org/10.1016/j.cardiores.2006.11.026.
[9] Y. Guo, W.J. Wu, Y. Qiu, X.L. Tang, Z. Yang, R. Bolli, Demonstration of an early and a late phase of ischemic preconditioning in mice, Am. J. Physiol. 275 (4) (Oct. 1998) H1375–H1387, https://doi.org/10.1152/ajpheart.1998.275.4.H1375.
[10] C.S. Filgueira, M.M. Bowden, B.C. Fallon, Investigating hypothyroidism and menopause as sex-specific health challenges affecting heart failure outcomes in a rodent infarct model, in: Presented at the Military Health System Research Symposium, Kissimmee, FL, Aug. 26, 2024.
[11] C.S. Filgueira, M.M. Bowden, B.C. Fallon, Impact of hormone replacement on cardiac function in a postmenopausal heart failure rat model, in: Presented at the American Heart Association Scientific Sessions 2024, Chicago, IL (USA), Nov. 16, 2024.
[12] F.-J. Neumann, et al., 2018 ESC/EACTS Guidelines on myocardial revascularization, Eur. Heart J. 40 (2) (Jan. 2019) 87–165, https://doi.org/10.1093/eurheartj/ehy394.
[13] K. Stergiopoulos, D.L. Brown, Initial coronary stent implantation with medical therapy vs medical therapy alone for stable coronary artery disease: meta-analysis of randomized controlled trials, Arch. Intern. Med. 172 (4) (Feb. 2012) 312–319, https://doi.org/10.1001/archinternmed.2011.1484.
[14] C. Zaragoza, et al., Animal models of cardiovascular diseases, J. Biomed. Biotechnol. 2011 (2011) 497841, https://doi.org/10.1155/2011/497841.
[15] A. Martino, et al., An insight into perfusion anisotropy within solid murine lung cancer tumors, Pharmaceutics 16 (8) (Aug. 2024) 8, https://doi.org/10.3390/pharmaceutics16081009.
[16] A. Corti, M. Colombo, F. Migliavacca, J.F. Rodriguez Matas, S. Casarin, C. Chiastra, Multiscale computational modeling of vascular adaptation: a systems biology approach using agent-based models, Front. Bioeng. Biotechnol. 9 (2021) 744560, https://doi.org/10.3389/fbioe.2021.744560.

[17] B. Feiger, et al., Accelerating massively parallel hemodynamic models of coarctation of the aorta using neural networks, Sci. Rep. 10 (1) (Jun. 2020) 9508, https://doi.org/10.1038/s41598-020-66225-0.
[18] D. Acharya, R.Y. Loyaga-Rendon, A. Chatterjee, I. Rajapreyar, K. Lee, Optical coherence tomography in cardiac allograft vasculopathy: state-of-the-art review, Circ. Heart Fail. 14 (9) (Sep. 2021) e008416, https://doi.org/10.1161/CIRCHEARTFAILURE.121.008416.
[19] V. Floré, et al., Intravascular ultrasound of the proximal left anterior descending artery is sufficient to detect early cardiac allograft vasculopathy, Clin. Transplant. 32 (2) (Feb. 2018), https://doi.org/10.1111/ctr.13167.
[20] C. Chiastra, et al., Healthy and diseased coronary bifurcation geometries influence near-wall and intravascular flow: a computational exploration of the hemodynamic risk, J. Biomech. 58 (Jun. 2017) 79–88, https://doi.org/10.1016/j.jbiomech.2017.04.016.
[21] G.S. Kassab, C.A. Rider, N.J. Tang, Y.C. Fung, Morphometry of pig coronary arterial trees, Am. J. Physiol. 265 (1 Pt 2) (Jul. 1993) H350–H365, https://doi.org/10.1152/ajpheart.1993.265.1.H350.
[22] T. Wischgoll, J.S. Choy, G.S. Kassab, Extraction of morphometry and branching angles of porcine coronary arterial tree from CT images, Am. J. Physiol. Heart Circ. Physiol. 297 (5) (Nov. 2009) H1949–H1955, https://doi.org/10.1152/ajpheart.00093.2009.
[23] G.S. Kassab, Y.C. Fung, Topology and dimensions of pig coronary capillary network, Am. J. Physiol. 267 (1 Pt 2) (Jul. 1994) H319–H325, https://doi.org/10.1152/ajpheart.1994.267.1.H319.
[24] G. De Nisco, et al., Comparison of swine and human computational hemodynamics models for the study of coronary atherosclerosis, Front. Bioeng. Biotechnol. 9 (2021) 731924, https://doi.org/10.3389/fbioe.2021.731924.
[25] A. Acuna, et al., Computational fluid dynamics of vascular disease in animal models, J. Biomech. Eng. 140 (8) (Aug. 2018) 808011–8080114, https://doi.org/10.1115/1.4039678.
[26] J. Suo, D.E. Ferrara, D. Sorescu, R.E. Guldberg, W.R. Taylor, D.P. Giddens, Hemodynamic shear stresses in mouse aortas: implications for atherogenesis, Arterioscler. Thromb. Vasc. Biol. 27 (2) (Feb. 2007) 346–351, https://doi.org/10.1161/01.ATV.0000253492.45717.46.
[27] A. Feintuch, et al., Hemodynamics in the mouse aortic arch as assessed by MRI, ultrasound, and numerical modeling, Am. J. Physiol. Heart Circ. Physiol. 292 (2) (Feb. 2007) H884–H892, https://doi.org/10.1152/ajpheart.00796.2006.
[28] Y. Huo, X. Guo, G.S. Kassab, The flow field along the entire length of mouse aorta and primary branches, Ann. Biomed. Eng. 36 (5) (May 2008) 685–699, https://doi.org/10.1007/s10439-008-9473-4.
[29] N. Mathuria, et al., Near-infrared sensitive nanoparticle-mediated photothermal ablation of ventricular myocardium, Heart Rhythm 19 (9) (Sep. 2022) 1550–1556, https://doi.org/10.1016/j.hrthm.2022.05.006.
[30] R. Terracciano, et al., Zonal intratumoral delivery of nanoparticles guided by surface functionalization, Langmuir 38 (45) (Nov. 2022) 13983–13994, https://doi.org/10.1021/acs.langmuir.2c02319.
[31] D.K. Wang, M. Rahimi, C.S. Filgueira, Nanotechnology applications for cardiovascular disease treatment: current and future perspectives, Nanomed. Nanotechnol. Biol. Med. 34 (Jun) (2021) 102387, https://doi.org/10.1016/j.nano.2021.102387.
[32] R. Terracciano, et al., Intratumoral gold nanoparticle-enhanced CT imaging: an in vivo investigation of biodistribution and retention, in: 2020 IEEE 20th International Conference on Nanotechnology (IEEE-NANO), Jul. 2020, pp. 349–353, https://doi.org/10.1109/NANO47656.2020.9183611.
[33] K. Keklikoglou, et al., Micro-CT for biological and biomedical studies: a comparison of imaging techniques, J. Imaging 7 (9) (Sep. 2021) 172, https://doi.org/10.3390/jimaging7090172.
[34] H. Wang, et al., Angiogenesis in tissue-engineered nerves evaluated objectively using MICROFIL perfusion and micro-CT scanning, Neural Regen. Res. 11 (1) (Jan. 2016) 168–173, https://doi.org/10.4103/1673-5374.175065.
[35] J.J. Weyers, D.D. Carlson, C.E. Murry, S.M. Schwartz, W.M. Mahoney, Retrograde perfusion and filling of mouse coronary vasculature as preparation for micro computed tomography imaging, J. Vis. Exp. (60) (Feb. 2012) e3740, https://doi.org/10.3791/3740.
[36] H. Kolesová, M. Bartoš, W.C. Hsieh, V. Olejníčková, D. Sedmera, Novel approaches to study coronary vasculature development in mice, Dev. Dyn. Off. Publ. Am. Assoc. Anat. 247 (8) (Aug. 2018) 1018–1027, https://doi.org/10.1002/dvdy.24637.
[37] R. Gharleghi, N. Chen, A. Sowmya, S. Beier, Towards automated coronary artery segmentation: a systematic review, Comput. Methods Progr. Biomed. 225 (Oct. 2022) 107015, https://doi.org/10.1016/j.cmpb.2022.107015.
[38] C. Chen, et al., Deep learning for cardiac image segmentation: a review, Front. Cardiovasc. Med. 7 (2020) 25, https://doi.org/10.3389/fcvm.2020.00025.
[39] D.A. Steinman, Image-based computational fluid dynamics modeling in realistic arterial geometries, Ann. Biomed. Eng. 30 (4) (Apr. 2002) 483–497, https://doi.org/10.1114/1.1467679.
[40] P.D. Morris, et al., Computational fluid dynamics modelling in cardiovascular medicine, Heart Br. Card. Soc. 102 (1) (Jan. 2016) 18–28, https://doi.org/10.1136/heartjnl-2015-308044.
[41] A.A. Ekmejian, et al., Advances in the computational assessment of disturbed coronary flow and wall shear stress: a contemporary review, J. Am. Heart Assoc. (Sep. 2024) e037129, https://doi.org/10.1161/JAHA.124.037129.
[42] C. Chiastra, et al., Computational fluid dynamics as supporting technology for coronary artery disease diagnosis and treatment: an international survey, Front. Cardiovasc. Med. 10 (Aug. 2023) 1216796, https://doi.org/10.3389/fcvm.2023.1216796.
[43] A. Candreva, et al., Current and future applications of computational fluid dynamics in coronary artery disease, Rev. Cardiovasc. Med. 23 (11) (Nov. 2022) 377, https://doi.org/10.31083/j.rcm2311377.
[44] U. Morbiducci, A.M. Kok, B.R. Kwak, P.H. Stone, D.A. Steinman, J.J. Wentzel, Atherosclerosis at arterial bifurcations: evidence for the role of haemodynamics and geometry, Thromb. Haemost. 115 (3) (Mar. 2016) 484–492, https://doi.org/10.1160/TH15-07-0597.
[45] P.A. Yushkevich, et al., User-guided 3D active contour segmentation of anatomical structures: significantly improved efficiency and reliability, Neuroimage 31 (3) (Jul. 2006) 1116–1128, https://doi.org/10.1016/j.neuroimage.2006.01.015.
[46] L. Antiga, M. Piccinelli, L. Botti, B. Ene-Iordache, A. Remuzzi, D.A. Steinman, An image-based modeling framework for patient-specific computational hemodynamics, Med. Biol. Eng. Comput. 46 (11) (Nov. 2008) 1097–1112, https://doi.org/10.1007/s11517-008-0420-1.
[47] G. Taubin, Curve and surface smoothing without shrinkage, in: Proceedings of IEEE International Conference on Computer Vision, Jun. 1995, pp. 852–857, https://doi.org/10.1109/ICCV.1995.466848.
[48] D. Gallo, et al., Cardiovascular morphometry with high-resolution 3D magnetic resonance: first application to left ventricle diastolic dysfunction, Med. Eng. Phys. 47 (Sep. 2017) 64–71, https://doi.org/10.1016/j.medengphy.2017.03.011.
[49] D. Gallo, D.A. Steinman, U. Morbiducci, An insight into the mechanistic role of the common carotid artery on the hemodynamics at the carotid bifurcation, Ann. Biomed. Eng. 43 (1) (Jan. 2015) 68–81, https://doi.org/10.1007/s10439-014-1119-0.
[50] L.M. Sangalli, P. Secchi, S. Vantini, A. Veneziani, Efficient estimation of three-dimensional curves and their derivatives by free-knot regression splines, applied to the analysis of inner carotid artery centrelines, J. R. Stat. Soc. Ser. C Appl. Stat. 58 (3) (Jul. 2009) 285–306, https://doi.org/10.1111/j.1467-9876.2008.00653.x.
[51] Q. Wang, H. Ouyang, L. Lv, L. Gui, S. Yang, P. Hua, Left main coronary artery morphological phenotypes and its hemodynamic properties, Biomed. Eng. Online 23 (1) (Jan. 2024) 9, https://doi.org/10.1186/s12938-024-01205-3.
[52] Girardeau-Montaut Daniel, CloudCompare. [Online]. Available: https://www.danielgm.net/cc/.
[53] J. Schindelin, et al., Fiji: an open-source platform for biological-image analysis, Nat. Methods 9 (7) (Jun. 2012) 676–682, https://doi.org/10.1038/nmeth.2019.
[54] M. Abbasian, M. Shams, Z. Valizadeh, A. Moshfegh, A. Javadzadegan, S. Cheng, Effects of different non-Newtonian models on unsteady blood flow hemodynamics in patient-specific arterial models with in-vivo validation, Comput. Methods Progr. Biomed. 186 (Apr. 2020) 105185, https://doi.org/10.1016/j.cmpb.2019.105185.
[55] J. Vogel, et al., Transgenic mice overexpressing erythropoietin adapt to excessive erythrocytosis by regulating blood viscosity, Blood 102 (6) (Sep. 2003) 2278–2284, https://doi.org/10.1182/blood-2003-01-0283.
[56] B.L. Walton, et al., Elevated hematocrit enhances platelet accumulation following vascular injury, Blood 129 (18) (May 2017) 2537–2546, https://doi.org/10.1182/blood-2016-10-746479.
[57] C.J. Hartley, A.K. Reddy, S. Madala, L.H. Michael, M.L. Entman, G.E. Taffet, Doppler estimation of reduced coronary flow reserve in mice with pressure overload cardiac hypertrophy, Ultrasound Med. Biol. 34 (6) (Jun. 2008) 892–901, https://doi.org/10.1016/j.ultrasmedbio.2007.11.019.
[58] B. Teng, S.L. Tilley, C. Ledent, S.J. Mustafa, In vivo assessment of coronary flow and cardiac function after bolus adenosine injection in adenosine receptor knockout mice, Phys. Rep. 4 (11) (Jun. 2016) e12818, https://doi.org/10.14814/phy2.12818.
[59] Y. Feng, et al., Bifurcation asymmetry of small coronary arteries in juvenile and adult mice, Front. Physiol. 9 (2018) 519, https://doi.org/10.3389/fphys.2018.00519.
[60] Y. Huo, G.S. Kassab, Intraspecific scaling laws of vascular trees, J. R. Soc. Interface 9 (66) (Jan. 2012) 190–200, https://doi.org/10.1098/rsif.2011.0270.
[61] D.J. Taylor, et al., Systematic review and meta-analysis of Murray's law in the coronary arterial circulation, Am. J. Physiol. Heart Circ. Physiol. 327 (1) (Jul. 2024) H182–H190, https://doi.org/10.1152/ajpheart.00142.2024.
[62] C.J. Hartley, A.K. Reddy, S. Madala, L.H. Michael, M.L. Entman, G.E. Taffet, Effects of isoflurane on coronary blood flow velocity in young, old and ApoE(-/-) mice measured by Doppler ultrasound, Ultrasound Med. Biol. 33 (4) (Apr. 2007) 512–521, https://doi.org/10.1016/j.ultrasmedbio.2006.11.002.
[63] D.N. Ku, D.P. Giddens, C.K. Zarins, S. Glagov, Pulsatile flow and atherosclerosis in the human carotid bifurcation. Positive correlation between plaque location and low oscillating shear stress, Arterioscler. Dallas Tex 5 (3) (1985) 293–302, https://doi.org/10.1161/01.atv.5.3.293.
[64] H.A. Himburg, D.M. Grzybowski, A.L. Hazel, J.A. LaMack, X.-M. Li, M. H. Friedman, Spatial comparison between wall shear stress measures and porcine arterial endothelial permeability, Am. J. Physiol. Heart Circ. Physiol. 286 (5) (May 2004) H1916–H1922, https://doi.org/10.1152/ajpheart.00897.2003.
[65] V. Peiffer, S.J. Sherwin, P.D. Weinberg, Computation in the rabbit aorta of a new metric - the transverse wall shear stress - to quantify the multidirectional character of disturbed blood flow, J. Biomech. 46 (15) (Oct. 2013) 2651–2658, https://doi.org/10.1016/j.jbiomech.2013.08.003.
[66] U. Morbiducci, et al., Wall shear stress topological skeleton independently predicts long-term restenosis after carotid bifurcation endarterectomy, Ann. Biomed. Eng. 48 (12) (Dec. 2020) 2936–2949, https://doi.org/10.1007/s10439-020-02607-9.
[67] D. Gallo, D.A. Steinman, P.B. Bijari, U. Morbiducci, Helical flow in carotid bifurcation as surrogate marker of exposure to disturbed shear, J. Biomech. 45 (14) (Sep. 2012) 2398–2404, https://doi.org/10.1016/j.jbiomech.2012.07.007.
[68] G. De Nisco, et al., The atheroprotective nature of helical flow in coronary arteries, Ann. Biomed. Eng. 47 (2) (Feb. 2019) 425–438, https://doi.org/10.1007/s10439-018-02169-x.

[69] X. Chen, et al., Growth, ageing and scaling laws of coronary arterial trees, J. R. Soc. Interface 12 (113) (Dec. 2015) 20150830, https://doi.org/10.1098/rsif.2015.0830.
[70] S.X. Vasquez, et al., Optimization of microCT imaging and blood vessel diameter quantitation of preclinical specimen vasculature with radiopaque polymer injection medium, PLoS One 6 (4) (Apr. 2011) e19099, https://doi.org/10.1371/journal.pone.0019099.
[71] L. Gan, J. Wikström, G. Bergström, B. Wandt, Non-invasive imaging of coronary arteries in living mice using high-resolution echocardiography, Scand. Cardiovasc. J. SCJ 38 (2) (May 2004) 121–126, https://doi.org/10.1080/14017430410029680.
[72] J. Chen, D.K. Ceholski, L. Liang, K. Fish, R.J. Hajjar, Variability in coronary artery anatomy affects consistency of cardiac damage after myocardial infarction in mice, Am. J. Physiol. Heart Circ. Physiol. 313 (2) (Aug. 2017) H275–H282, https://doi.org/10.1152/ajpheart.00127.2017.
[73] S.T. Haworth, J.H. Linehan, T.A. Bronikowski, C.A. Dawson, A hemodynamic model representation of the dog lung, J. Appl. Physiol. 70 (1) (Jan. 1991) 15–26, https://doi.org/10.1152/jappl.1991.70.1.15. Bethesda Md 1985.
[74] J.F. Gross, M. Intaglietta, B.W. Zweifach, Network model of pulsatile hemodynamics in the microcirculation of the rabbit omentum, Am. J. Physiol. 226 (5) (May 1974) 1117–1123, https://doi.org/10.1152/ajplegacy.1974.226.5.1117.
[75] P.D. Weinberg, C. Ross Ethier, Twenty-fold difference in hemodynamic wall shear stress between murine and human aortas, J. Biomech. 40 (7) (2007) 1594–1598, https://doi.org/10.1016/j.jbiomech.2006.07.020.
[76] W.R. Dean, XVI. *Note on the motion of fluid in a curved pipe*, London, Edinburgh Dublin Phil. Mag. J. Sci. 4 (20) (Jul. 1927) 208–223, https://doi.org/10.1080/14786440708564324.
[77] S. Sankaran, H.J. Kim, G. Choi, C.A. Taylor, Uncertainty quantification in coronary blood flow simulations: impact of geometry, boundary conditions and blood viscosity, Cardiovasc. Biomech. Health Dis. 49 (12) (Aug. 2016) 2540–2547, https://doi.org/10.1016/j.jbiomech.2016.01.002.
[78] M. Lodi Rizzini, et al., Modelling coronary flows: impact of differently measured inflow boundary conditions on vessel-specific computational hemodynamic profiles, Comput. Methods Progr. Biomed. 221 (Jun. 2022) 106882, https://doi.org/10.1016/j.cmpb.2022.106882.
[79] M. Sarti, et al., Deep learning for automated analysis of cellular and extracellular components of the foreign body response in multiphoton microscopy images, Front. Bioeng. Biotechnol. 9 (2021) 797555, https://doi.org/10.3389/fbioe.2021.797555.
[80] E. Serafini, A. Corti, D. Gallo, C. Chiastra, X.C. Li, S. Casarin, An agent-based model of cardiac allograft vasculopathy: toward a better understanding of chronic rejection dynamics, Front. Bioeng. Biotechnol. 11 (2023) 1190409, https://doi.org/10.3389/fbioe.2023.1190409.